methods communications

Acta Cryst F
STRUCTURAL BIOLOGY
COMMUNICATIONS

ISSN 2053-230X

Crystal structure determination of the armadillo repeat domain of *Drosophila* SARM1 using MIRAS phasing

Weixi Gu,[a,b,c]‡ Zhenyao Luo,[a,b,c]*‡ Clemens Vonrhein,[d] Xinying Jia,[a,e] Thomas Ve,[f] Jeffrey D. Nanson[a,b,c] and Bostjan Kobe[a,b,c]*

[a]School of Chemistry and Molecular Biosciences, The University of Queensland, St Lucia, Brisbane, Queensland 4072, Australia, [b]Institute for Molecular Bioscience, The University of Queensland, St Lucia, Brisbane, Queensland 4072, Australia, [c]Australian Infectious Diseases Research Centre, The University of Queensland, St Lucia, Brisbane, Queensland 4072, Australia, [d]Global Phasing Ltd, Cambridge CB3 OAX, United Kingdom, [e]Centre for Advanced Imaging, The University of Queensland, St Lucia, Brisbane, Queensland 4072, Australia, and [f]Institute for Glycomics, Griffith University, Southport, Queensland 4222, Australia. *Correspondence e-mail: uqzluo1@uq.edu.au, b.kobe@uq.edu.au

Received 7 February 2021
Accepted 29 June 2021

Edited by M. A. Hough, University of Essex, United Kingdom

‡ These authors contributed equally to this work.

Keywords: armadillo repeat; *Drosophila* SARM1; nicotinamide mononucleotide; X-ray crystallography; multiple isomorphous replacement; anomalous scattering; phase combination.

PDB reference: armadillo repeat domain of *Drosophila* SARM1, 7lcz

Supporting information: this article has supporting information at journals.iucr.org/f

The crystal structure determination of the armadillo repeat motif (ARM) domain of *Drosophila* SARM1 (dSARM1$^{\rm ARM}$) is described, which required the combination of a number of sources of phase information in order to obtain interpretable electron-density maps. SARM1 is a central executioner of programmed axon degeneration, a common feature of the early phase of many neurodegenerative diseases. SARM1 is held in the inactive state in healthy axons by its N-terminal auto-inhibitory ARM domain, and is activated to cleave NAD upon injury, triggering subsequent axon degeneration. To characterize the molecular mechanism of SARM1 activation, it was sought to determine the crystal structure of the SARM1 ARM domain. Here, the recombinant production and crystallization of dSARM1$^{\rm ARM}$ is described, as well as the unconventional process used for structure determination. Crystals were obtained in the presence of NMN, a precursor of NAD and a potential activator of SARM1, only after *in situ* proteolysis of the N-terminal 63 residues. After molecular-replacement attempts failed, the crystal structure of dSARM1$^{\rm ARM}$ was determined at 1.65 Å resolution using the MIRAS phasing technique with *autoSHARP*, combining data from native, selenomethionine-labelled and bromide-soaked crystals. The structure will further the understanding of SARM1 regulation.

1. Introduction

The protein SARM1 (sterile alpha and Toll/interleukin-1 receptor motif-containing 1) is a central executioner of injury-induced axon degeneration (Wallerian degeneration). Loss of SARM1 protects axons from degeneration for weeks after injury induced by axotomy or vincristine (Osterloh *et al.*, 2012; Gerdts *et al.*, 2013). In healthy axons, SARM1 is held in the inactive state by the N-terminal armadillo repeat motif (ARM) domain. Upon injury, this auto-inhibition is relieved, permitting the C-terminal TIR (Toll/interleukin-1 receptor) domains to hydrolyze nicotinamide adenine dinucleotide (NAD) into nicotinamide and either ADP-ribose (ADPR) or cyclic ADPR (cADPR) (Essuman *et al.*, 2017; Horsefield *et al.*, 2019). These changes in turn trigger an influx of Ca^{2+} into the cells, a corresponding loss of ATP and eventually axon degeneration (Loreto *et al.*, 2015; Horsefield *et al.*, 2019). Despite its important role in this process, the mechanism of SARM1 activation is poorly understood. Recently, it has been suggested that the accumulation of the NAD precursor nicotinamide mononucleotide (NMN) is a trigger of SARM1

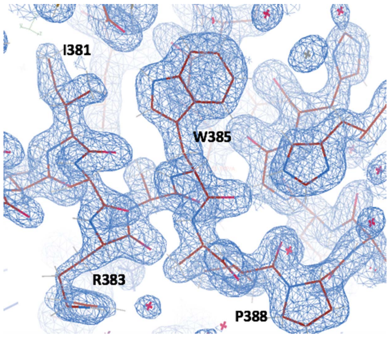

activation, resulting in subsequent axon degeneration (Di Stefano *et al.*, 2015). Therefore, we hypothesized that NMN may interact with the ARM domain and reverse the ARM domain-mediated auto-inhibition.

To determine crystal structures, the phase components of the structure factors, which are lost during diffraction data collection, need to be recovered. In the case where similar protein structures are available, one can use molecular replacement (Rossmann, 1990). Alternatively, one can locate the positions of heavy atoms (HAs) that are either incorporated into the crystals or already present within the macromolecule through techniques such as MIR (multiple isomorphous replacement), usually with the inclusion of the anomalous signal, and SAD (single-wavelength anomalous dispersion) (Vijayan & Ramaseshan, 2001).

We sought to determine the crystal structure of the NMN-bound ARM domain of *Drosophila* SARM1 (dSARM1$^{\rm ARM}$), which would greatly enhance our understanding of the mechanism of NMN-induced relief of ARM domain-mediated auto-inhibition in SARM1. We crystallized dSARM1$^{\rm ARM}$ in the NMN-bound state. Although the crystals diffracted X-rays to high resolution (1.65 Å), attempts to determine the phases using the molecular-replacement technique were not successful. We then attempted SAD phasing using the anomalous signals from bromide or selenium, which were separately incorporated into the crystals. However, the anomalous signal present in either the Br-SAD or the Se-SAD data set was weak and initial phases could not be successfully estimated. The phase problem was eventually solved by employing the MIRAS (multiple isomorphous replacement with anomalous scattering) method with *autoSHARP* (Vonrhein *et al.*, 2007), combining the data from native, selenomethionine (SeMet)-labelled and bromide-soaked crystals. Here, we report the protein production, crystallization and structure determination of dSARM1$^{\rm ARM}$, and present our experience as a case study of modern MIRAS phasing.

2. Materials and methods

2.1. Protein production

The cDNA encoding dSARM1$^{\rm ARM}$ (residues 307–678; UniProtKB Q6IDD9) was codon-optimized for expression in *Escherichia coli* and was cloned into the pMCSG7 expression vector at the SspI site using the ligation-independent cloning technique (forward primer 5′-TACTTCCAATCCAATGCGAATGGACAGATGTTGAAGCTTGCGGATTTGAAATTAGACG-3′; reverse primer 5′-TTATCCACTTCCAATGTTACGTTTCCCCAATTAAGCGCAGCGCTTGGG-3′; Aslanidis & de Jong, 1990; Eschenfeldt *et al.*, 2009). The plasmid was transformed into *E. coli* BL21 (DE3) (for the native protein) or B834 (DE3) (for the SeMet-labelled protein) cells by heat shock. The cells were grown on lysogeny broth (LB) agar plates containing 100 µg ml^{-1} ampicillin at 37°C overnight. Colonies were inoculated into 10 ml LB medium containing 100 µg ml^{-1} ampicillin and were incubated at 37°C and 225 rev min^{-1} overnight. To produce the native protein, 1 ml of the LB overnight culture of transformed *E. coli* BL21 (DE3) cells was inoculated into 1000 ml auto-induction medium (Studier, 2005) containing 100 µg ml^{-1} ampicillin and incubated at 37°C and 225 rev min^{-1} until the OD$_{600}$ reached 0.8–1.0. The temperature was then decreased to 20°C for overnight protein expression. To produce the SeMet-labelled protein, 1 ml of the overnight LB culture of transformed *E. coli* B834 (DE3) cells was inoculated into 1000 ml M9 minimal medium containing 1× M9 salt (33.7 m*M* Na_2HPO_4, 22 m*M* KH_2PO_4, 8.55 m*M* NaCl, 9.35 m*M* NH_4Cl), 1× trace elements solution (0.13 m*M* EDTA, 0.03 m*M* $FeCl_3$, 6.2 µ*M* $ZnCl_2$, 0.76 µ*M* $CuCl_2$, 0.42 µ*M* $CoCl_2$, 1.62 µ*M* H_3BO_3, 0.08 µ*M* $MnCl_2$), 0.4%(*v*/*v*) glucose, 1 m*M* $MgSO_4$, 0.3 m*M* $CaCl_2$, 1× BME vitamin solution (Sigma–Aldrich) and 100 µg ml^{-1} ampicillin. The bacteria were grown at 37°C and 22 rev min^{-1} until the OD$_{600}$ reached 0.8–1.0. The temperature was then decreased to 20°C for a 30 min incubation. 1 ml 50 mg ml^{-1} SeMet (Sigma–Aldrich) was added to 1000 ml culture. Expression was induced by adding isopropyl β-D-1-thiogalactopyranoside (IPTG) to a final concentration of 1 m*M* and the cells were incubated overnight at 20°C and 225 rev min^{-1}. The *E. coli* BL21 (DE3) or B834 (DE3) cells were harvested by centrifugation at 6000*g* for 20 min at 4°C and were treated identically in subsequent purification steps.

The harvested cells were resuspended in lysis buffer (50 m*M* HEPES pH 8.0, 500 m*M* NaCl, 30 m*M* imidazole, 1 m*M* DTT). Phenymethylsulfonyl fluoride was added to the cell suspension to a final concentration of 1 m*M*. The cells were subsequently lysed by sonication. The lysed cells were centrifuged at 15 300*g* for 40 min at 4°C. The supernatant was loaded onto a 5 ml HisTrap HP column (Cytiva) equilibrated with lysis buffer. The bound target protein was washed with 100 ml lysis buffer and eluted with elution buffer (50 m*M* HEPES pH 8.0, 500 m*M* NaCl, 300 m*M* imidazole, 1 m*M* DTT) on an ÄKTApurifier (Cytiva). Fractions containing dSARM1$^{\rm ARM}$ were combined and incubated with Tobacco etch virus (TEV) protease (20:1 protein:TEV protease ratio) in SnakeSkin Dialysis Tubing (3.5 kDa molecular-weight cutoff; Thermo Fisher Scientific) and dialyzed against buffer consisting of 20 m*M* HEPES pH 8.0, 300 m*M* NaCl, 1 m*M* DTT at 4°C overnight. The His$_6$-tag-removed protein was reloaded onto a 5 ml HisTrap HP column to remove uncleaved fusion protein and free His$_6$ tag. The flowthrough was then collected, concentrated to a volume of 10 ml and injected onto a Superdex 75 HiLoad 26/600 column (Cytiva) equilibrated with gel-filtration buffer (10 m*M* HEPES pH 8.0, 150 m*M* NaCl, 1 m*M* DTT). The peak fractions containing pure dSARM1$^{\rm ARM}$ were pooled, concentrated using a 30 kDa molecular-weight cutoff Amicon Ultra Centrifugal filter (Millipore), flash-frozen and stored at −80°C.

2.2. Crystallization

Prior to crystallization, dSARM1$^{\rm ARM}$ protein (17 mg ml^{-1}) was incubated with NMN in a 1:10 protein:compound molar ratio at 4°C overnight. Sparse-matrix protein crystallization

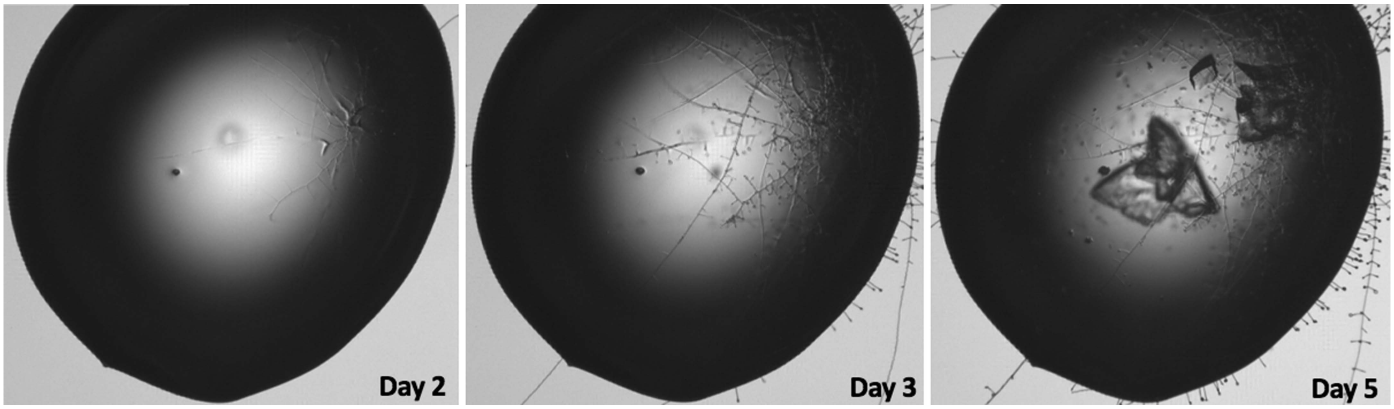

Figure 1
Crystal growth of NMN-bound dSARM1^{ARM}. Crystals were observed after five days in 0.1 *M* SPG buffer pH 8.0, 25%(*w*/*v*) PEG 1500 in the presence of fungal cells.

screening was performed using the commercially available Index (Hampton Research), Combined Synergy (Hampton Research), PEG/Ion (Hampton Research), PEGRx (Hampton Research), JCSG+ (Molecular Dimensions), PACT *premier* (Molecular Dimensions), ProPlex (Molecular Dimensions) and ShotGun (Molecular Dimensions) screens. Crystallization trials were set up using a Mosquito liquid-handling robot (TTP LabTech) in a 96-well hanging-drop plate format with 100 nl protein solution and 100 nl reservoir solution per drop equilibrated against 75 µl reservoir solution at 20°C. To scale up the drop sizes, hanging drops consisting of 2 µl NMN-bound protein and 2 µl commercial reservoir solution were equilibrated against 500 µl homemade reservoir solution consisting of 0.1 *M* SPG buffer (succinic acid, sodium dihydrogen phosphate and glycine in a 2:7:7 molar ratio, pH 8.0) and 25%(*w*/*v*) PEG 1500 at 20°C. The SeMet-labelled crystals were produced using the same crystallization condition as for the native crystals. Crystals were observed in the crystallization drops after 3–5 days. SDS–PAGE and mass spectrometric analyses of these crystals were performed to ascertain the identity of the crystallized protein.

2.3. Diffraction data collection and processing

Prior to flash-cooling in liquid nitrogen, crystals of NMN-bound native dSARM1^{ARM} and SeMet-labelled dSARM1^{ARM} were cryoprotected in a cryoprotectant solution consisting of 0.1 *M* SPG buffer pH 8.0, 25%(*w*/*v*) PEG 1500, 25%(*v*/*v*) PEG 400. Crystals derivatized with bromide were prepared by soaking the native crystals in the mother liquor containing 0.5 *M* sodium bromide, 25%(*v*/*v*) PEG 400 for 2 min prior to flash-cooling. All data sets were collected on the MX2 beamline at the Australian Synchrotron using an EIGER X 16M detector (Aragão *et al.*, 2018). The native data set was collected at a wavelength of 0.95372 Å, the SeMet-labelled data set was collected at the theoretical selenium absorption edge with a wavelength of 0.97857 Å and the bromide-soaked data set was collected at the theoretical bromine absorption edge with a wavelength of 0.91976 Å. Diffraction data from NMN-bound dSARM1^{ARM} crystals (native, SeMet-labelled and bromide-soaked data) were processed and analyzed with *autoPROC* (Vonrhein *et al.*, 2011). Initial phases were calculated using the MIRAS technique with *autoSHARP* (Vonrhein *et al.*, 2007). The structure was refined using the strategy of TLS parameters with iterations of *phenix.refine* (Afonine *et al.*, 2012) and manual model building in *Coot* (Emsley *et al.*, 2010).

3. Results and discussion

The boundaries of the expression constructs for dSARM1^{ARM} were determined based on sequence alignments among human, mouse, *Caenorhabditis elegans* and *Drosophila* SARM1, taking secondary-structure predictions into consideration. Small-scale expression tests were performed to identify constructs producing soluble target protein. Using the dSARM1$^{ARM307–678}$ construct, we successfully expressed soluble dSARM1^{ARM} protein, with a final yield of 10 mg per litre of bacterial culture.

During sparse-matrix screening, we observed (after five days) the growth of a few crystals in 0.1 *M* SPG buffer pH 8.0, 25%(*w*/*v*) PEG 1500 (PACT *premier* condition A5) at 20°C. The crystals were chunky but irregular in shape (Fig. 1). However, despite our best efforts, we were not able to reproduce the NMN-bound dSARM1^{ARM} crystals using homemade crystallization solutions. Importantly, we observed that what appeared to be fungal cells, possibly *Penicillium*, grew in the crystallization drop prior to the growth of the dSARM1^{ARM} crystals (Fig. 1). SDS–PAGE analysis of the NMN-bound dSARM1^{ARM} crystals, followed by mass spectrometry, indicated that the crystallized protein corresponded to residues 370–678 of SARM1 (*i.e.* lacking the N-terminal 63 amino acids). This led us to reason that partial proteolysis, mediated by proteases secreted by the fungal cells, was required for the crystallization of NMN-bound SARM1^{ARM}. We therefore attempted *in situ* proteolysis using the proteases trypsin and chymotrypsin, but did not obtain any crystals. We also constructed dSARM1$^{ARM370–678}$ with the hope of solving the crystal reproducibility issues. However, this construct

Table 1
Data-processing statistics from *XDS* and *AIMLESS*.

The statistics are based on the calculations from *AIMLESS*. Values in parentheses are for the highest resolution shell.

	Native	Bromide-soaked	SeMet-labelled
Space group	$P1$	$P1$	$P1$
a, b, c (Å)	38.95, 50.82, 76.12	39.12, 51.15, 75.83	38.86, 50.28. 75.18
α, β, γ (°)	103.52, 101.89, 95.23	103.37, 101.51, 96.67	104.88, 101.37, 94.89
Resolution (Å)	48.9–1.74 (1.78–1.74)	46.59–2.01 (2.06–2.01)	48.1–4.18 (4.67–4.18)
$R_{\rm merge}$†	0.058 (0.472)	0.067 (0.621)	0.036 (0.043)
$R_{\rm meas}$‡	0.068 (0.554)	0.077 (0.719)	0.051 (0.060)
$R_{\rm p.i.m.}$§	0.035 (0.288)	0.038 (0.357)	0.036 (0.043)
Mean $I/\sigma(I)$	17.6 (3.4)	17.8 (3.2)	21.7 (19.9)
$CC_{1/2}$	0.999 (0.931)	0.999 (0.830)	0.98 (0.96)
Total No. of observations	3386169 (19534)	284357 (19417)	13961 (3827)
No. of unique observations	54045 (2793)	35879 (2561)	3835 (1074)
Completeness (%)	96.3 (89.2)	97.9 (93.5)	97.9 (96.8)
Multiplicity	7.1 (7.0)	7.9 (7.6)	3.6 (3.6)
Anomalous completeness (%)	95.4 (85.5)	95.3 (88.5)	92.6 (89.4)
Anomalous multiplicity	3.5 (3.6)	3.9 (3.9)	1.8 (1.9)
DelAnom correlation between half-sets	−0.091 (0.076)	0.398 (0.053)	0.297 (0.183)
Mid-slope of anomalous normal probability	0.956	1.173	1.392

† $R_{\rm merge} = \sum_{hkl}\sum_i |I_i(hkl) - \langle I(hkl)\rangle| / \sum_{hkl}\sum_i I_i(hkl)$. ‡ $R_{\rm meas} = \sum_{hkl}\{N(hkl)/[N(hkl)-1]\}^{1/2}\sum_i |I_i(hkl) - \langle I(hkl)\rangle| / \sum_{hkl}\sum_i I_i(hkl)$. § $R_{\rm p.i.m.} = \sum_{hkl}\{1/[N(hkl)-1]\}^{1/2} \times \sum_i |I_i(hkl) - \langle I(hkl)\rangle| / \sum_{hkl}\sum_i I_i(hkl)$.

failed to yield soluble protein. Crystals only grew when the original crystallization solution containing the fungal cells was added to the homemade crystallization solution. For these reasons, we had a limited number of crystals to optimize our diffraction experiments.

A native data set was collected from NMN-bound dSARM1$^{\rm ARM}$ crystals on the MX2 beamline at the Australian Synchrotron. The data were initially processed using *XDS* (Kabsch, 2010) and *AIMLESS* (Evans & Murshudov, 2013). The crystals diffracted to ∼1.7 Å resolution, with strong ice rings appearing at ∼1.9, 2.3 and 3.9 Å (Table 1, Fig. 2). The crystal had the symmetry of space group $P1$ and was likely to contain two dSARM1$^{\rm ARM}$ molecules in the asymmetric unit, with a Matthews coefficient of 2.07 Å^3 Da^{-1} and a solvent content of 40%.

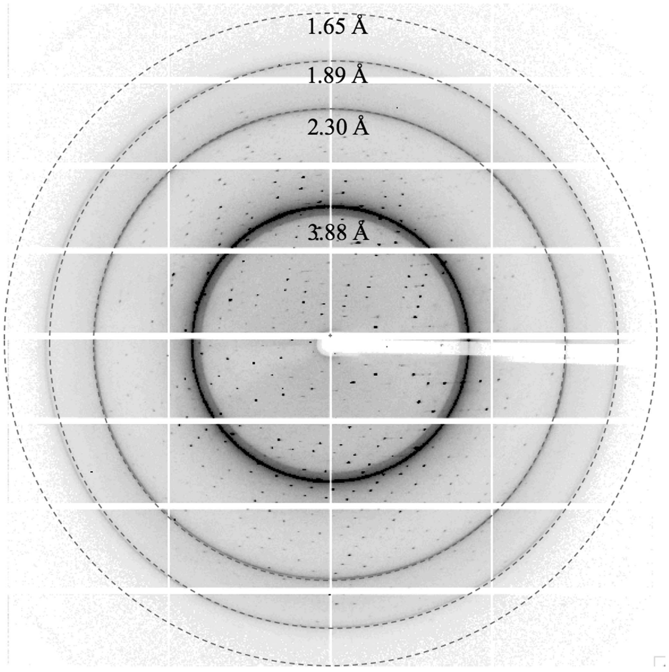

Figure 2
A representative diffraction image of an NMN-bound dSARM1$^{\rm ARM}$ crystal. The crystal diffracted X-rays to >1.65 Å resolution.

ARM domains are protein-interaction domains that are found in many proteins displaying diverse cellular roles from gene expression to cytoskeleton regulation (Coates, 2003). They typically consist of tandem repeats of armadillo motifs. One armadillo motif contains ∼42 residues, which fold into three α-helices (H1, H2 and H3). Stacking of these motifs forms a right-handed superhelix with an elongated concave surface, characterized by parallel H3 helices arranged in a ladder fashion (Coates, 2003). Initially, we attempted to solve the structure of dSARM1$^{\rm ARM}$ by molecular replacement. We used the available ARM structures, such as importin-α (PDB entry 1ial; Kobe, 1999) and Vac8p (PDB entry 5xjg; Jeong *et al.*, 2017), with various modifications, as search models within *Phaser* (McCoy *et al.*, 2007). We attempted automated molecular replacement with *MrBUMP* (Keegan & Winn, 2008) and *BALBES* (Long *et al.*, 2008), as well as *ab initio* macromolecular phasing with *ARCIMBOLDO* (Rodríguez *et al.*, 2009). However, we did not obtain any clear solutions using these approaches. Post-mortem analysis of the structures revealed that the dSARM1$^{\rm ARM}$ crystal structure adopted a curled conformation, which is drastically different from other existing ARM structures, with a root-mean-square deviation (r.m.s.d.) of the backbone C$^{\alpha}$ atoms of greater than 3.5 Å between them.

We alternatively sought to solve the phase problem by SAD phasing. To this end, we incorporated bromide (through soaking) and, separately, SeMet (during expression) into the protein crystals and collected anomalous data sets to ∼2.0 and 4.2 Å resolution, respectively, using X-ray wavelengths close to the absorption edges of the respective HAs (Table 1). Unfortunately, the crystals were prone to radiation damage, as demonstrated by the reduction in diffraction quality and a sharply decreasing Wilson *B* factor. Due to the low *P*1 symmetry, data sets with high multiplicity and therefore accurately determined anomalous differences, which are often required for successful SAD phasing, could not be acquired. Also, as we only had access to a limited number of crystals, merging multiple low-multiplicity data sets was not a viable option. The bromide data set had an anomalous multiplicity of ∼3.9, whereas the SeMet data set had an even lower anomalous multiplicity of merely 1.8. Data processing using *XDS* (Kabsch, 2010) and *AIMLESS* (Evans & Murshudov, 2013) indicated that the values of the mid-slope of anomalous normal probabilities of the bromide and SeMet data sets were 1.17 and 1.39, respectively, suggesting that detectable but weak anomalous signal was present in these two data sets. Using a CC_{ano} cutoff of 0.15, the detectable anomalous signals were up to 2.7 and 4.2 Å resolution for the bromide and SeMet data sets, respectively (Fig. 3), but subsequent searches for HAs in *AutoSol* within *Phenix* (Terwilliger *et al.*, 2009) and *CRANK*2 within *CCP*4*i*2 (Skubák & Pannu, 2013; Potterton *et al.*, 2018) invariably failed.

Fortunately, the bromide-soaked and SeMet-labelled crystals had similar unit-cell dimensions and the same space group as the native protein crystals (Table 1). Both HA data sets also shared relatively low *R* factors and a high correlation coefficient (CC) compared with the native data at low to intermediate resolutions (∼2.6 Å; Fig. 4), thus making MIRAS or SIRAS (single isomorphous replacement with anomalous scattering) phasing a possibility. During the 2019 CCP4/Shanghai Workshop we were able to use the *autoPROC* software package for data reprocessing (Vonrhein *et al.*, 2011),

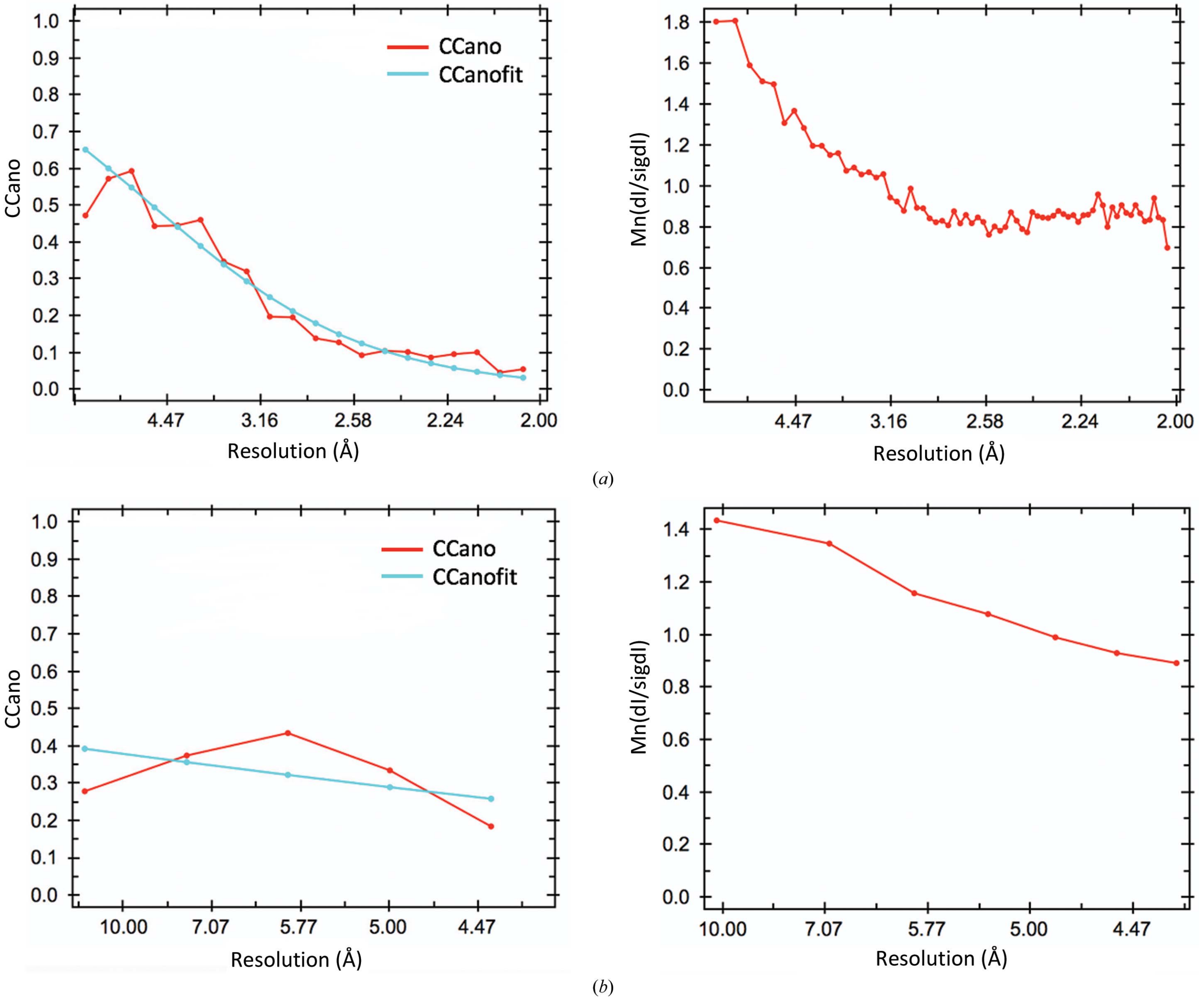

(*a*)

(*b*)

Figure 3
Analysis of the anomalous signals using *AIMLESS* (manual). (*a*) CCano (left) and Mn(dI/sigdI) (right) as a function of resolution for the bromide data set. (*b*) CCano (left) and Mn(dI/sigdI) (right) as a function of resolution for the SeMet data set. The figures were automatically generated during manual data processing using *AIMLESS*.

which uses *XDS* for data processing (Kabsch, 2010), *POINTLESS* for space-group determination (Evans, 2006), *AIMLESS* for scaling (Evans & Murshudov, 2013) and *STARANISO* for analysis of diffraction anisotropy (Vonrhein *et al.*, 2011), plus multiple additional tools for diffraction-image processing (Table 2, Fig. 5). Careful processing of the diffraction images is important, as diffraction outliers are damaging to the success of the HA search. We inspected the diffraction images to redefine accurate beam-stop masks for all of the data sets and subtracted ice rings from the diffraction data in *autoPROC*. In the SeMet data set, we observed four pixels with extremely high intensities, with coordinates (1675, 2512) at ~6.2 Å, (5, 3182) at ~1.6 Å, (21, 1668) at ~1.7 Å and (1765, 2531) at ~6.7 Å, respectively, that appeared in all diffraction images of the data set. Successful indexing of the SetMet data set was only achieved when these bad pixels were removed from the diffraction images using the image-analysis and inspection tool in *autoPROC* (`aP_detect_damaged_pixels`). We assume that these pixels accumulated damage over time and should therefore always be included in the detector pixel mask that defines inactive pixels and regions. Importantly, our SetMet data set also suffered from anisotropy, and within initial scaling using *AIMLESS*, an isotropic resolution cutoff of 4.2 Å was chosen. However, using

Native data to bromide data

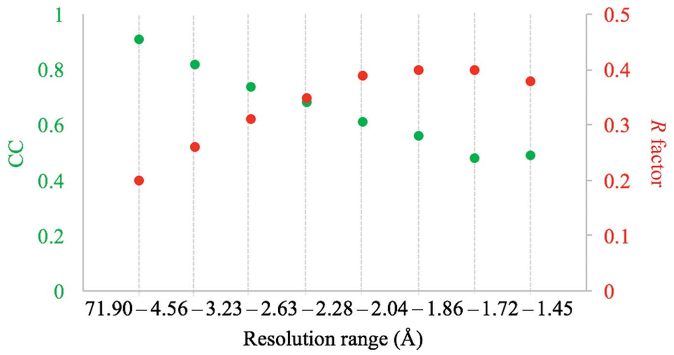

Resolution range (Å)	71.9 – 4.56	– 3.23	– 2.63	– 2.28	– 2.04	– 1.86	– 1.72	– 1.45
***R* factor**	0.20	0.26	0.31	0.35	0.39	0.40	0.40	0.38
CC	0.91	0.82	0.74	0.68	0.61	0.56	0.48	0.49

Native data to SeMet data

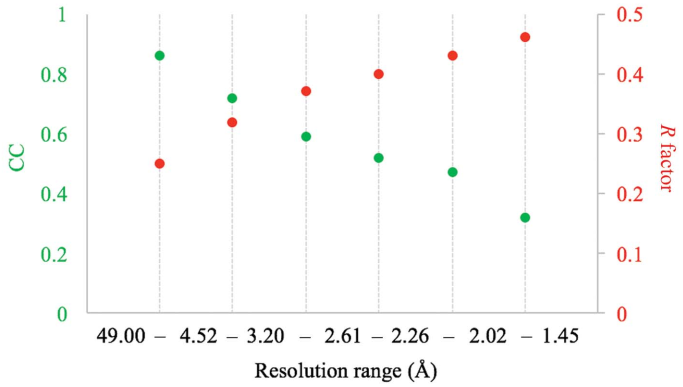

Resolution range (Å)	49.0 – 4.52	– 3.20	– 2.61	– 2.26	– 2.02	– 1.45
***R* factor**	0.25	0.32	0.37	0.40	0.43	0.46
CC	0.86	0.72	0.59	0.52	0.47	0.32

Figure 4
Analysis of isomorphorism of the native, bromide-soaked and SeMet-labelled crystals. The statistics (*R* factor and CC on amplitudes) were generated within *autoPROC* using the native data as a reference (`check_indexing -v`).

Table 2
Data-processing statistics from *autoPROC* and refinement statistics from *Phenix*.

The statistics are based on the calculations from *autoPROC* and *MolProbity*. Values in parentheses are for the highest resolution shell.

	Native	Bromide-soaked	SeMet-labelled
Data collection			
Space group	*P*1	*P*1	*P*1
a, *b*, *c* (Å)	38.92, 50.79, 76.05	39.07, 51.08, 75.73	38.89, 50.31, 75.22
α, β, γ (°)	103.52, 101.90, 95.26	103.38, 101.52, 96.66	104.86, 101.36, 94.91
Resolution (Å)	71.9–1.46 (1.60–1.46)	49.0–1.68 (1.82–1.68)	48.1–1.89 (2.11–1.89)
$R_{\rm merge}$†	0.05 (0.95)	0.08 (1.77)	0.07 (0.76)
$R_{\rm meas}$‡	0.06 (1.15)	0.09 (2.05)	0.09 (1.08)
$R_{\rm p.i.m.}$§	0.03 (0.63)	0.04 (1.01)	0.07 (0.76)
Mean $I/\sigma(I)$	15.9 (1.6)	13.9 (1.0)	9.2 (1.2)
$CC_{1/2}$	1.00 (0.63)	1.00 (0.4)	1.00 (0.47)
Total reflections	456719 (20265)	393818 (19421)	86502 (4041)
Unique reflections	64028 (3201)	48934 (2447)	24291 (1216)
Completeness (spherical) (%)	67.2 (14.2)	78.2 (19.1)	56.6 (10.0)
Completeness (ellipsoidal) (%)	83.5 (40.3)	90.0 (44.7)	85.3 (38.8)
Multiplicity	7.1 (6.3)	8.0 (7.9)	3.6 (3.3)
Anomalous completeness (spherical) (%)	66.5 (14.0)	76.4 (18.5)	55.8 (9.7)
Anomalous completeness (ellipsoidal) (%)	82.7 (39.8)	87.9 (43.4)	84.1 (38.0)
Anomalous multiplicity	3.6 (3.2)	4.1 (4.1)	1.8 (1.7)
Refinement			
Resolution (Å)	37.67–1.65 [native data set]		
$R_{\rm work}$¶	0.21		
$R_{\rm free}$¶	0.23		
R.m.s.d., bonds (Å)	0.002		
R.m.s.d., angles (°)	0.47		
Ramachandran favoured (%)	98.51		
Ramachandran outliers (%)	0.33		
Rotamer outliers (%)	0.19		
Clashscore	1.64		
Average *B* factor (Å^2)	27.77		
C^{β} outliers	0		

† $R_{\rm merge} = \sum_{hkl}\sum_i |I_i(hkl) - \langle I(hkl)\rangle| / \sum_{hkl}\sum_i I_i(hkl)$. ‡ $R_{\rm meas} = \sum_{hkl}\{N(hkl)/[N(hkl)-1]\}^{1/2} \sum_i |I_i(hkl) - \langle I(hkl)\rangle| / \sum_{hkl}\sum_i I_i(hkl)$. § $R_{\rm p.i.m.} = \sum_{hkl}\{1/[N(hkl)-1]\}^{1/2} \sum_i |I_i(hkl) - \langle I(hkl)\rangle| / \sum_{hkl}\sum_i I_i(hkl)$. ¶ $R_{\rm work} = \sum_{hkl} \big||F_{\rm obs}| - |F_{\rm calc}|\big| / \sum_{hkl} |F_{\rm obs}|$; $R_{\rm free}$ is equivalent to $R_{\rm work}$, with 5% of data excluded from refinement process. $|F_{\rm obs}|$ and $|F_{\rm calc}|$ represent the observed and calculated structure-factor amplitudes, respectively.

STARANISO in *autoPROC*, the significant data that were previously excluded during scale determination in *AIMLESS* because of anisotropy could now be accounted for, extending the diffraction limit of the data set to 1.9 Å.

For MIRAS phasing and initial model building, we used *autoSHARP* (Vonrhein *et al.*, 2007), which uses *SHELXC*/*D* for substructure determination (Schneider & Sheldrick, 2002), *SHARP* for HA refinement, phasing and substructure completion (de La Fortelle & Bricogne, 1997), *SOLOMON* for density modification (Abrahams & Leslie, 1996) and *Buccaneer* for automatic model building (Cowtan, 2006). After multiple attempts to choose an appropriate resolution cutoff to maximize the phasing power, phase determination was eventually performed using data with a resolution cutoff of 25–2.5 Å. The high-resolution cutoff seems slightly counterintuitive, because it is (i) much higher than the HA signal (isomorphous difference and anomalous signal) in the different data sets and (ii) lower than the overall diffraction limit of the available data sets. However, in cases where the difference between these two resolution limits (HA signal and overall) is rather large it is often beneficial to restrict the data to 2.5–3 Å resolution in the early stages of the structure-solution process. At this stage, one is mainly interested in achieving a successful substructure determination, a clear indication of the correct enantiomorph (during the density-modification step) and hopefully some meaningful secondary-structure elements resulting from the automatic model-building step. All of these can easily be achieved by using 2.5–3 Å resolution data. If even higher resolution data are used at this stage, the initial low-resolution phase information (which is expected to be poor) might be inadequate in helping density modification to bridge the large resolution range to the full limit of the available data, at least within the density-modification and phase-extension procedure using *SOLOMON* as implemented in *autoSHARP*. During HA detection, where combinations of SIR(AS) (native plus bromide or native plus SeMet data sets) and SAD (bromide or SeMet data set alone) were tried, *autoSHARP* calculates the CC between the observed and calculated normalized substructure amplitudes *E*. The solution with the highest CC(*E*), and therefore the initial substructure solution most likely to be successful, corresponded to SIRAS using the SeMet data set [CC(*E*) = 0.188 with four SeMet sites out of the expected ten sites in the asymmetric unit]. Using this solution as a starting point, *SHARP* within *autoSHARP* refined the coordinates, occupancy and temperature factors for the initial HA sites as well as scaling non-isomorphism parameters between the three data sets. It further detected ten bromide sites (overall phasing power of 0.216 for isomorphous differences and 0.483 for anomalous differences, with the phasing power dropping below 1 at 24.42 and 5.48 Å, resolution, respectively) and ten SeMet sites (overall phasing power of 0.136 for isomorphous differences and 0.299 for anomalous differences, with the phasing power dropping below 1 at 24.42 and 4.92 Å resolution, respectively). These values were consistent with the analysis of the anomalous signal from the data-processing stages and confirmed that the HA signal (and the initial maps computed with these phases) would present a rather low-resolution starting point for subsequent steps. A final set of phases was calculated in both hands and the most likely enantiomorph was determined by performing a single cycle of solvent flipping in *SOLOMON* as part of *autoSHARP*, suggesting that the correct phases were those from the inverted hand, based on its slightly higher score (a combination of the CC between observed E^2 values and the E^2 values of the modified map and the contrast in the assigned protein and solvent regions) of 0.1234 (two molecules in the asymmetric unit) compared with 0.1078 from the original hand. After multiple cycles of density modification to optimize the solvent content, the best density-modified map with a score of 1.8697 was finally handed over to *Buccaneer*, which managed to build a total of 614 residues in two chains (out of the expected 618 residues for a dimer in the asymmetric unit). Consistently, the ten SeMet sites, including the initial four sites during HA detection, have been shown to be consistent with the (Se)Met residues built by *Buccaneer* within the initial model. This was the final result of a fully automatic *autoSHARP* run (starting with the data sets, the sequence, information about the scattering properties of the heavy atoms in the different data sets and some indication of the expected number of bromide sites) and provided the starting point for subsequent steps. Further manual model building in *Coot* (Emsley *et al.*, 2010) and refinement against the native data using *phenix.refine* (Afonine *et al.*, 2012) improved the quality of the phases (Fig. 6). For refinement, we restricted the data resolution to 1.65 Å, as opposed to using the full resolution range of the anisotropically analysed *STARANISO* data. We observed that the data at 1.45–1.65 Å resolution contained greater than 40% phase error and less than 80% data completeness. Excluding the data at 1.45–1.65 Å resolution

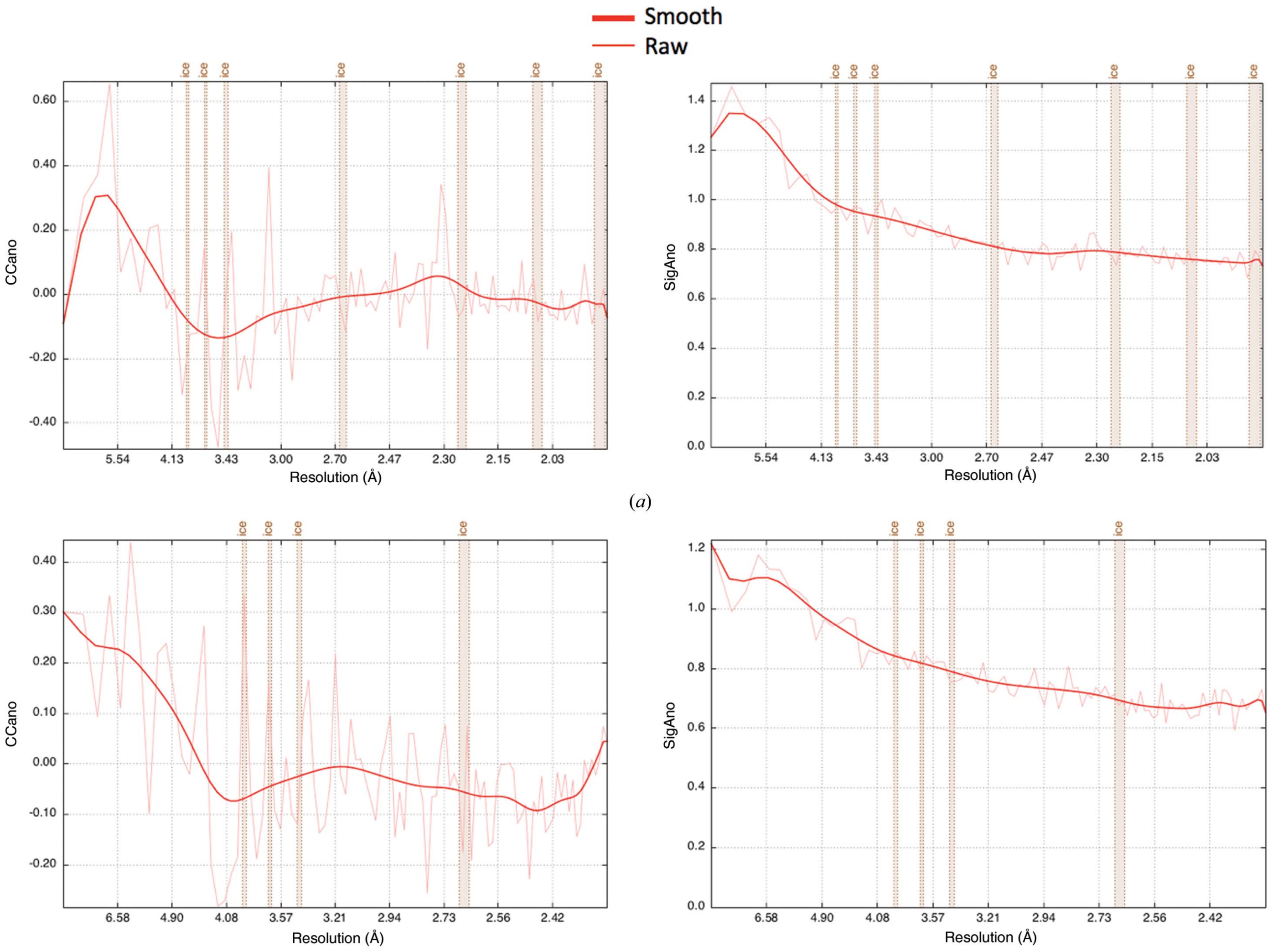

(*a*)

(*b*)

Figure 5
Analysis of the anomalous signals using *autoPROC*. (*a*) CCano (left) and SigAno (right) as a function of resolution for the bromide data set. (*b*) CCano (left) and SigAno (right) as a function of resolution for the SeMet data set. The figures were automatically generated during data processing with *autoPROC*. SigAno corresponds to Mn(dI/sigdI) in Fig. 3.

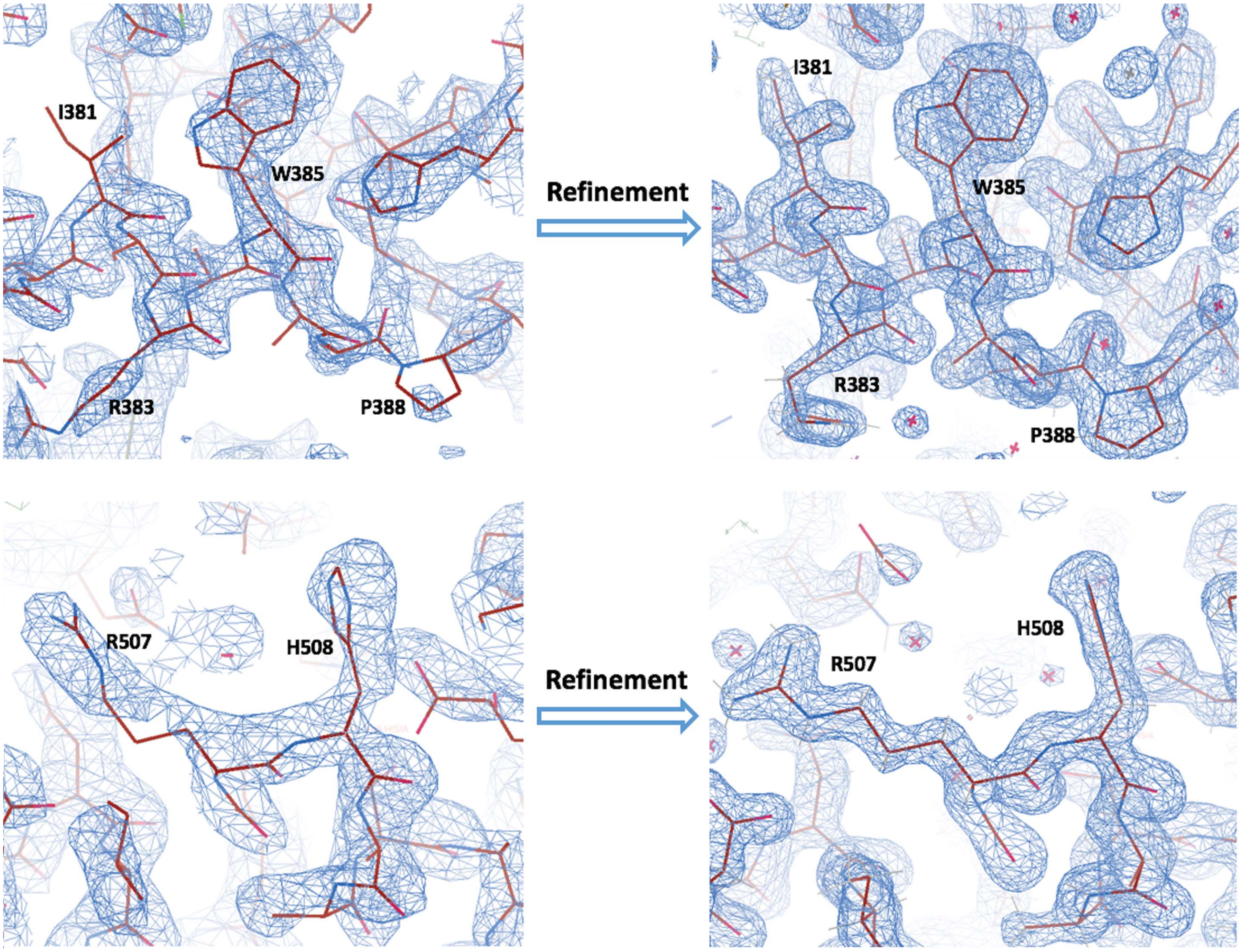

Figure 6
Representative electron-density maps, contoured at 1.5σ, before and after refinement. The panels on the left show the initial electron-density map ($2F_o - F_c$) calculated using the MIRAS-based phases from *autoSHARP* after density modification (*SOLOMON*) and model building (*Buccaneer*) at a resolution of 2.5 Å. The panels on the right show the electron-density map in the corresponding region after refinement with *phenix.refine* at 1.65 Å resolution.

indeed resulted in a clearer overall electron-density map. The final structure was determined with $R_{\rm work}$ and $R_{\rm free}$ values of 0.21 and 0.23, respectively (Table 2).

4. Summary

In conclusion, we describe the crystal structure determination of dSARM1$^{\rm ARM}$ as an illustrative example of how a number of technical difficulties in the process can be overcome. Multiple nonconventional steps were employed here. Firstly, *in situ* proteolysis allowed diffraction-quality crystals to be obtained in the first place. Secondly, after attempts to solve the phase problem by molecular replacement failed, heavy atoms were introduced by bromide soaking and SeMet incorporation. However, neither of these SAD data sets provided sufficient anomalous signal to obtain interpretable electron-density maps. The low symmetry of the crystal system provided little opportunity to collect high-multiplicity multiwavelength data sets around the Se and Br edges, which might have helped substructure detection within each bromide or SeMet data set. However, after careful data processing (manual beam-stop masking, exclusion of damaged pixels that are not yet in the detector mask and handling of ice rings) using *autoPROC* and combining the resulting improved data from the native, bromide-soaked and SeMet-labelled crystals, the MIRAS approach as implemented in *autoSHARP* led to interpretable electron-density maps and a clear initial starting model. The structure of NMN-bound dSARM1$^{\rm ARM}$ displays a more compact conformation, differing from the canonical ARM domains, with an r.m.s.d. on backbone C$^{\alpha}$ atoms of over 3.5 Å. This could explain why molecular replacement failed to solve the phase problem. This structure will help us to understand the molecular mechanisms of regulation of SARM1, a protein with a central role in neurodegenerative disease. The biological implications of the structure are discussed in Figley *et al.* (2021).

Acknowledgements

We acknowledge the use of the University of Queensland Remote Operation Crystallization and X-ray (UQROCX) Facility at the Centre for Microscopy and Microanalysis and the support from the staff, Dr Gordon King and Karl Byriel. We acknowledge the use of the Australian Synchrotron MX beamlines, part of ANSTO, including the Australian Cancer Research Foundation detector, and the support of the staff. We also thank the CCP4/Shanghai 2019 workshop, their organisers, including CCP4, Dr Ruslan Sanishvili, National Facility for Protein Science in Shanghai, Shanghai Tech University iHuman Institute and Shanghai Synchrotron Radiation Facility, and Professor Gérard Bricogne from Global Phasing Ltd for the help with structure determination. We are grateful to Dr Gayle Petersen for diligent proofreading and discussion of the manuscript.

Funding information

This work was supported by grants from the Australian National Health and Medical Research Council (NHMRC; grants 1107804 and 1160570 to BK and TV, 1071659 to BK and 1108859 to TV) and the Australian Research Council (ARC; Laureate Fellowship FL180100109 to BK). TV received ARC Discovery Early Career Researcher Award (DECRA) funding (DE170100783).

References

Abrahams, J. P. & Leslie, A. G. W. (1996). *Acta Cryst.* D**52**, 30–42.

Afonine, P. V., Grosse-Kunstleve, R. W., Echols, N., Headd, J. J., Moriarty, N. W., Mustyakimov, M., Terwilliger, T. C., Urzhumtsev, A., Zwart, P. H. & Adams, P. D. (2012). *Acta Cryst.* D**68**, 352–367.

Aragão, D., Aishima, J., Cherukuvada, H., Clarken, R., Clift, M., Cowieson, N. P., Ericsson, D. J., Gee, C. L., Macedo, S., Mudie, N., Panjikar, S., Price, J. R., Riboldi-Tunnicliffe, A., Rostan, R., Williamson, R. & Caradoc-Davies, T. T. (2018). *J. Synchrotron Rad.* **25**, 885–891.

Aslanidis, C. & de Jong, P. J. (1990). *Nucleic Acids Res.* **18**, 6069–6074.

Coates, J. C. (2003). *Trends Cell Biol.* **13**, 463–471.

Cowtan, K. (2006). *Acta Cryst.* D**62**, 1002–1011.

Di Stefano, M., Nascimento-Ferreira, I., Orsomando, G., Mori, V., Gilley, J., Brown, R., Janeckova, L., Vargas, M. E., Worrell, L. A., Loreto, A., Tickle, J., Patrick, J., Webster, J. R. M., Marangoni, M., Carpi, F. M., Pucciarelli, S., Rossi, F., Meng, W., Sagasti, A., Ribchester, R. R., Magni, G., Coleman, M. P. & Conforti, L. (2015). *Cell Death Differ.* **22**, 731–742.

Emsley, P., Lohkamp, B., Scott, W. G. & Cowtan, K. (2010). *Acta Cryst.* D**66**, 486–501.

Eschenfeldt, W. H., Lucy, S., Millard, C. S., Joachimiak, A. & Mark, I. D. (2009). *Methods Mol. Biol.* **498**, 105–115.

Essuman, K., Summers, D. W., Sasaki, Y., Mao, X., DiAntonio, A. & Milbrandt, J. (2017). *Neuron*, **93**, 1334–1343.

Evans, P. (2006). *Acta Cryst.* D**62**, 72–82.

Evans, P. R. & Murshudov, G. N. (2013). *Acta Cryst.* D**69**, 1204–1214.

Figley, M. D., Gu, W., Nanson, J. D., Shi, Y., Sasaki, Y., Cunnea, K., Malde, A. K., Jia, X., Luo, Z., Saikot, F. K., Mosaiab, T., Masic, V., Holt, S., Hartley-Tassell, L., McGuinness, H. Y., Manik, M. K., Bosanac, T., Landsberg, M. J., Kerry, P. S., Mobli, M., Hughes, R. O., Milbrandt, J., Kobe, B., DiAntonio, A. & Ve, T. (2021). *Neuron*, **109**, 1118–1136.

Gerdts, J., Summers, D. W., Sasaki, Y., DiAntonio, A. & Milbrandt, J. (2013). *J. Neurosci.* **33**, 13569–13580.

Horsefield, S., Burdett, H., Zhang, X., Manik, M. K., Shi, Y., Chen, J., Qi, T., Gilley, J., Lai, J. S., Rank, M. X., Casey, L. W., Gu, W., Ericsson, D. J., Foley, G., Hughes, R. O., Bosanac, T., von Itzstein, M., Rathjen, J. P., Nanson, J. D., Boden, M., Dry, I. B., Williams, S. J., Staskawicz, B. J., Coleman, M. P., Ve, T., Dodds, P. N. & Kobe, B. (2019). *Science*, **365**, 793–799.

Jeong, H., Park, J., Kim, H. I., Lee, M., Ko, Y. J., Lee, S., Jun, Y. & Lee, C. (2017). *Proc. Natl Acad. Sci. USA*, **114**, E4539–E4548.

Kabsch, W. (2010). *Acta Cryst.* D**66**, 125–132.

Keegan, R. M. & Winn, M. D. (2008). *Acta Cryst.* D**64**, 119–124.

Kobe, B. (1999). *Nat. Struct. Biol.* **6**, 388–397.

La Fortelle, E. de & Bricogne, G. (1997). *Methods Enzymol.* **276**, 472–494.

Long, F., Vagin, A. A., Young, P. & Murshudov, G. N. (2008). *Acta Cryst.* D**64**, 125–132.

Loreto, A., Di Stefano, M., Gering, M. & Conforti, L. (2015). *Cell. Rep.* **13**, 2539–2552.

McCoy, A. J., Grosse-Kunstleve, R. W., Adams, P. D., Winn, M. D., Storoni, L. C. & Read, R. J. (2007). *J. Appl. Cryst.* **40**, 658–674.

Osterloh, J. M., Yang, J., Rooney, T. M., Fox, A. N., Adalbert, R., Powell, E. H., Sheehan, A. E., Avery, M. A., Hackett, R., Logan, M. A., MacDonald, J. M., Ziegenfuss, J. S., Milde, S., Hou, Y. J., Nathan, C., Ding, A., Brown, R. H., Conforti, L., Coleman, M., Tessier-Lavigne, M., Züchner, S. & Freeman, M. R. (2012). *Science*, **337**, 481–484.

Potterton, L., Agirre, J., Ballard, C., Cowtan, K., Dodson, E., Evans, P. R., Jenkins, H. T., Keegan, R., Krissinel, E., Stevenson, K., Lebedev, A., McNicholas, S. J., Nicholls, R. A., Noble, M., Pannu, N. S., Roth, C., Sheldrick, G., Skubak, P., Turkenburg, J., Uski, V., von Delft, F., Waterman, D., Wilson, K., Winn, M. & Wojdyr, M. (2018). *Acta Cryst.* D**74**, 68–84.

Rodríguez, D. D., Grosse, C., Himmel, S., González, C., de Ilarduya, I. M., Becker, S., Sheldrick, G. M. & Usón, I. (2009). *Nat. Methods*, **6**, 651–653.

Rossmann, M. G. (1990). *Acta Cryst.* A**46**, 73–82.

Schneider, T. R. & Sheldrick, G. M. (2002). *Acta Cryst.* D**58**, 1772–1779.

Skubák, P. & Pannu, N. S. (2013). *Nat. Commun.* **4**, 2777.

Studier, F. W. (2005). *Protein Expr. Purif.* **41**, 207–234.

Terwilliger, T. C., Adams, P. D., Read, R. J., McCoy, A. J., Moriarty, N. W., Grosse-Kunstleve, R. W., Afonine, P. V., Zwart, P. H. & Hung, L.-W. (2009). *Acta Cryst.* D**65**, 582–601.

Vijayan, M. & Ramaseshan, S. (2001). *International Tables for Crystallography*, Vol. B, edited by U. Shmueli, pp. 264–275. Dordrecht: Springer.

Vonrhein, C., Blanc, E., Roversi, P. & Bricogne, G. (2007). *Methods Mol. Biol.* **364**, 215–230.

Vonrhein, C., Flensburg, C., Keller, P., Sharff, A., Smart, O., Paciorek, W., Womack, T. & Bricogne, G. (2011). *Acta Cryst.* D**67**, 293–302.